

Memristor-Based Image Enhancement: High Efficiency and Robustness

Ruohua Zhu, Zhiri Tang, Shizhuo Ye^{ID}, *Student Member, IEEE*, Qijun Huang^{ID}, Lijun Guo, and Sheng Chang^{ID}, *Senior Member, IEEE*

Abstract—Due to many outstanding physical characteristics, memristors have attracted much attention from all over the world. As a tendency, memristor-based systems are beginning to be applied in various fields of image processing, such as pattern recognition and edge detection. For the first time, memristors are introduced to image enhancement in this work, which dexterously processes the images twice via memristors' intrinsic properties. Adopting a coarse transmission map and nonlinear memristive characteristics, the algorithm is highly efficient, which enormously reduces the computational cost, and image quality assessment demonstrates that it maintains comparable performance with classical algorithms. Furthermore, the temperature effect and the memristor instability, namely, the device-to-device variations and the cycle-to-cycle variations, are taken into consideration, and the average of several stacked images is proven effective in relieving the influence of variations. We believe that this work can explore a new application for the memristor.

Index Terms—Image enhancement, memristor, robustness, temperature effect, variations.

I. INTRODUCTION

NOWADAYS, high-performance computing on hardware has become a strong cornerstone for some fascinating functions. With the growth of chip size and power consumption of system, traditional “Von Neumann” architecture has restricted the development of large-scale calculations, such as real-time image processing, and the further development of the computation-centric calculations [1]–[3]. To settle this problem, various devices are put forward to realize in-memory computing. Among them, memristor [4]–[10] is one of the

Manuscript received November 15, 2020; revised December 13, 2020; accepted December 15, 2020. Date of publication December 31, 2020; date of current version January 22, 2021. This work was supported in part by the National Natural Science Foundation of China under Grant 62004062, Grant 62074116, Grant 61874079, and Grant 81971702; in part by the Wuhan Research Program of Application Foundation under Grant 20180104010 11289; and in part by the Luojia Young Scholars Program. The review of this article was arranged by Editor R. Kuroda. (*Corresponding author: Sheng Chang.*)

Ruohua Zhu and Lijun Guo are with the School of Physics and Electronics, Henan University, Kaifeng 475004, China.

Zhiri Tang is with the School of Physics and Technology, Wuhan University, Wuhan 430072, China, and also with the Department of Computer Science, City University of Hong Kong, Hong Kong.

Shizhuo Ye, Qijun Huang, and Sheng Chang are with the School of Physics and Technology, Wuhan University, Wuhan 430072, China (e-mail: changsheng@whu.edu.cn).

Color versions of one or more figures in this article are available at <https://doi.org/10.1109/TED.2020.3045684>.

Digital Object Identifier 10.1109/TED.2020.3045684

most potential substituents for its simple structure with small device footprint, multilevel memristive states, high integration of computation and storage, low write energy and standby power, and so on. Moreover, memristors have appropriate write energy and standby power, where the write energy of most resistive random access memory (RRAM) and pulse-code modulation (PCM) devices [1] are around $100 \sim 10$ and $10 \sim 100$ pJ, respectively. Some works had proved that the computational energy efficiency of memristors exceeded those of today's graphical processing units by two orders of magnitude [11].

The high-density and low-power characteristics of memristor crossbars facilitate their applications in image processing. Existing articles about memristor-based image processing employed memristors simply, such as demonstrating image compression using multilevel, stable states of the memristors [10], and the algorithm roughly introducing the memristors in one tiny step [12]. Furthermore, to obtain good performance, some traditional image enhancement algorithms, such as the dehazing algorithms by Tan and Oakley [13], Tan [14], Tarel *et al.* [15], Nishino *et al.* [16], He *et al.* [17], Meng *et al.* [18], and Sulami *et al.* [19], had to pay the cost of relatively heavy calculation burden. Up until now, there is a big margin for memristors' image processing.

Image enhancement is an important area of image processing. To pursue a more vivid visual feast by improving the image quality or enrich the quantity of information from an unsatisfactory image, image enhancement purposefully emphasizes the peculiarity of the whole image or part of it, strengthening the interpretation and recognition effect. Unfortunately, complex calculations are normally needed in image enhancement. For the first time, memristors are introduced to image enhancement in this article. A novel memristor-based image enhancement (MIEA) is presented to simplify the calculation process by taking advantage of the memristive characteristics. A compact memristor model [20], [21] that described the formation and annihilation of conductive filaments (CFs) is used to support a vivid portrait of memristive characteristics. Two steps are executed to implement the MIEA: 1) transmission map is processed by the memristors relieving influence of the depth of field and 2) original image is processed by the memristors expanding the range of pixel values. In addition, considering the consistency difficulty in memristors' fabrication, the robustness of MIEA has been

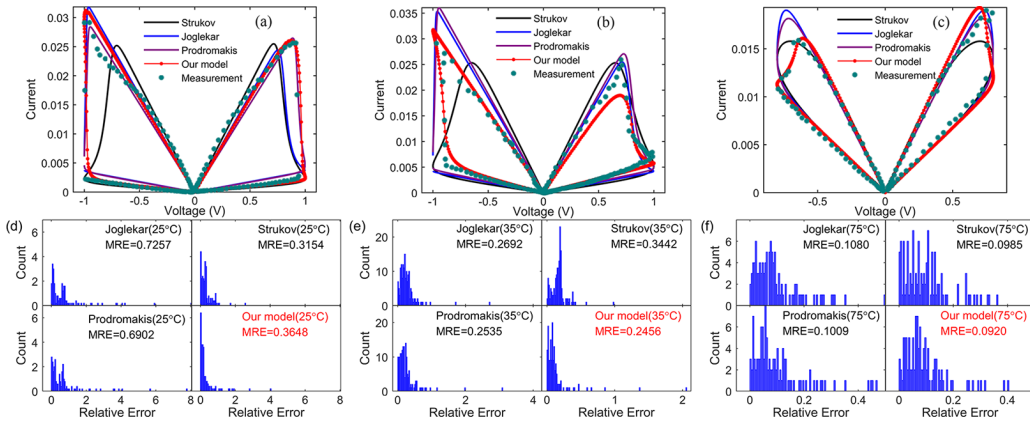


Fig. 1. Comparisons of several compact memristor models (“Our model” [20], “Measurement” [27], “Joglekar” [28], “Prodromakis” [29], and “Strukov” [30]), which describes the I - V curve of Ni/NiO/Ni memristor [27] at the temperatures (a) 25 °C, (b) 35 °C, and (c) 75 °C, and the count of relative errors (d), (e), and (f).

discussed through the discussion of temperature effect and stability of memristors. Experimental results show that the MIEA has an outstanding performance. By the virtue of full exploitation of memristive characteristics, we hope that our algorithm paves a new way of memristors-based image processing.

In this article, the contents are arranged as follows. Section II discusses a modified nonlinear memristor model. Section III gives a detailed process and structure of MIEA and quantitatively assesses its validity. Section IV discusses temperature effect and memristive variations on MIEA. Section V presents the conclusions.

II. MODIFIED NONLINEAR MEMRISTOR MODEL

A. Modified Memristor Model

Several pivotal articles had illustrated that the CFs played an essential role in the switching mechanisms in the memristors [22]–[24], and various memristor models were constructed. Thereinto, a versatile and accurate memristor model [20] based on the equivalent resistor topology of the variable CFs issued a vivid description of basic physical nature of CFs’ change with a unified and simple mathematical expression as in the following equation:

$$M = \frac{1}{\sum_{i=1}^N \frac{1}{NR_{OFF} - N \cdot c_i \cdot (\alpha + \beta e^{\int_0^t \lambda \cdot v(t) dt} + \gamma_0)} (R_{OFF} - R_{ON})} \quad (1)$$

where $v(t)$, N , R_{ON} , R_{OFF} , and c_i are the input voltage over time t , the number of conductive channels, the smallest memristance, the largest memristance, and a statistical distribution of CFs’ lengths, respectively. α , β , γ , and γ_0 describe states of CFs’ and their dynamic process.

Due to the voltage polarity in the initial electroforming process, the uncontrollable process of the CFs’, the vertical drift and electromigration along with the conductive channel [25], and so on, memristors showed asymmetric bipolar switching behaviors [26]. To improve the versatile and accuracy of the above memristor model, the $\gamma_0(v(t)) = (1 + \tanh(5v(t)))/2 \cdot \gamma_{0_1} + \gamma_{0_2}$ is redefined to consistent with the asymmetry memristive characteristics, where

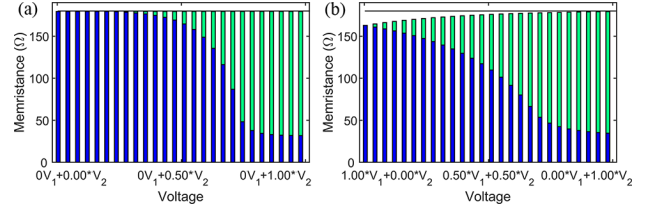


Fig. 2. Memristors are initiated at the maximum memristance (M_{max}). (a) and (b) Change of the memristances (the blue bars) with the same initial states (the green bars) under various voltages ($[0^* V_2, 1.00^* V_2]$, $[1^* V_1 + 0^* V_2, 0^* V_1 + 1^* V_2]$).

$\gamma_0(v(t)) = \gamma_{0_2}$ ($v(t) \ll 0$) and $\gamma_0(v(t)) = \gamma_{0_1} + \gamma_{0_2}$ ($v(t) \gg 0$). $\gamma_0(v(t))$ is used to fine-tune the growth speed of the CFs, and $(1 + \tanh(5v(t)))/2$, which has continuous high-order derivative, is used to control different CFs’ growth speeds under the voltages $v(t)$ of differing polarity.

In this article, the model is used to describe the Ni/NiO/Ni memristor [27] under three different temperatures (25 °C, 35 °C, and 75 °C). $\theta = 0.5$ and $\alpha = 0$ are set to ensure that there is no initial conductive layer and the initial lengths of the CFs are about 0. $\lambda = 8.2$ and $\beta = 3.7$ are used to modulate the dynamic switching process. $(\gamma_{0_1}, \gamma_{0_2})$ are set as $(-2.2, -5)$, $(-4.8, -4)$, $(0.8, -7.2)$ at the 25 °C, 35 °C, and 75 °C, as shown in Fig. 1(a)–(c).

To test our model’s precision, Fig. 1(a)–(c) provides the comparisons of several compact memristor models (“Our model” [20], “Measurement” [27], “Joglekar” [28], “Prodromakis” [29], and “Strukov” [30]). From that, one can see that our model matches the measurement data very well at different temperatures. What is more, from a set of quantitative analysis, as shown in Fig. 1(d)–(f), one can conclude that, compared with other memristor models, our model apparently has the greater number of the relative errors centralizing around zero and the smaller mean relative errors (MREs). Summarily, the improved memristor model can much more accurately describe the asymmetric I - V characteristics of the Ni/NiO/Ni memristor at different temperatures.

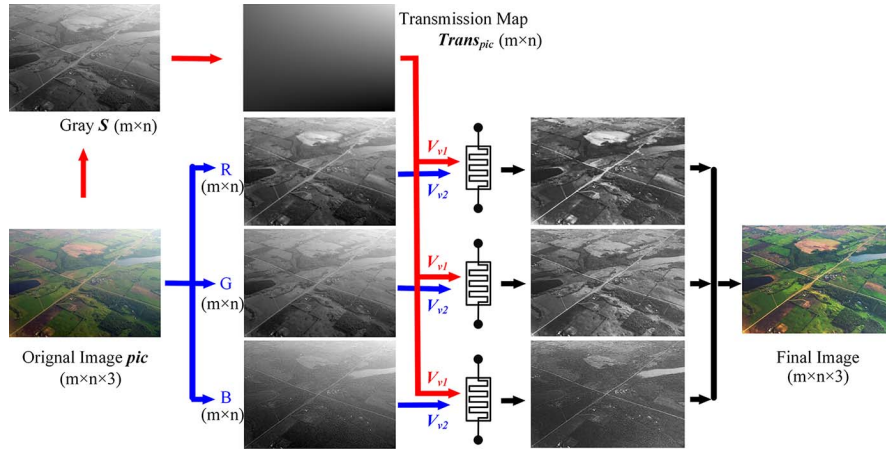


Fig. 3. Overview of MIEA: (1) the memristor crossbars are first fine-tuned by the transmission map (red routes) and (2) the memristor crossbars are second modulated by the original image (blue routes). The final image is obtained by normalizing currents.

B. Nonlinear Memristive Characteristics

As is well known, the memristor has nonlinear $I-V$ characteristics. This attractive memristive characteristic can realize the zoom function through the mapping between the input voltage and the output current. To obtain the change of memristances, the voltages are first applied to adjust memristances, and a small voltage is used to extract memristances without changing memristive states. It is noteworthy that the MIEA essentially originates from the nonlinear dynamics of the memristor, existing either during the gradual RESET process or during the gradual SET process. In this article, the gradual SET process is interpreted as follows.

In Fig. 2(a), when the voltages ($[0*V_2, 0.4*V_2], [0.4*V_2, 0.75*V_2], [0.75*V_2, 1.00*V_2]$) are applied, memristances change from the same initial resistance state to differing final resistance states, which distribute in a small, large, and small ranges, respectively. This simple mapping relationship depends entirely on the physical switching mechanisms of the memristor, and to better control the voltage-memristance mapping relationship, two correlative voltages V_1 and V_2 are applied successively to alter the memristances in Fig. 2(b). The combination of voltages V_2 -related V_1 and V_2 , namely the complex coding scheme for the V_2 , shapes an extensive mapping relationship, which is introduced in the following image enhancement.

III. MEMRISTOR-BASED IMAGE ENHANCEMENT

Images that are shot in bad conditions are usually lacking clarity due to complex mediums in the atmosphere. Some classical traditional dehazing algorithms [13]–[15], [17] removed the fog's influence by combining transmission map with the original image, miraculously reconstructing the image and performing a large amount of computation at the same time. To reduce the amount of calculation, based on the atmospheric light model [14], [31], the MIEA is proposed here for its brief and effective calculation in this section.

A. Algorithm and Structure of MIEA

Take an RGB image as an example to introduce the overview of MIEA using memristors at 75 °C, as shown in Fig. 3.

- 1) The minimum memristance is M_{\min} , and the memristor crossbars **Mem** ($m \times n \times 3$) are initiated at the maximum memristance (M_{\max}).
- 2) The RGB image **pic** ($m \times n \times 3$) is converted to a gray-scale image **S** ($m \times n$). A transmission map **Trans(pic)** ($m \times n$) is derived from the gray-scale image **S**.
- 3) The transmission map **Trans(pic)** ($m \times n$) is linearly coded as the appropriate voltages V_{v1} ($m \times n$, $V_{v1} = \text{param}_a \cdot \text{Trans(pic)} / 255$), which is applied to memristor crossbars **Mem** ($m \times n \times 3$) three times: first adjusting the memristances and aiming to eliminate the fogging density's effect. Here, param_a is a fitting constant.
- 4) The red, green, and blue channels from RGB image ($m \times n \times 3$) are linearly coded as the appropriate voltages V_{v2} ($m \times n \times 3$ and $V_{v2} = \text{param}_b \cdot \text{pic} / 255$), which are applied to the memristor crossbars **Mem** ($m \times n \times 3$), where param_b is a fitting constant.
- 5) A set of constant voltages V_s ($m \times n \times 3$) are applied on the memristor crossbars **Mem** without affecting memristances [26], and the currents are obtained and normalized in the range [$V_s/M_{\max}, V_s/M_{\min}$], which is a form of the final image.

In a haze image, the worst distortion usually appears in the top part, where the light is not scattered and cannot reach the camera [17], resulting in that the pixels are restricted to a narrow range. The worse the distortions in an image are, the narrower the range of the pixels is restricted to. In this article, the minimum pixel in each corner (4 pixels) of the image **S** is extracted, and they are linearly interpolated to form a simplified transmission map. The coarse transmission map is used to roughly and effectively describe the depth of field and brightness in a haze image, and its brief calculating process reduces the computational complexity.

B. Experiment Results

The images (Highway [19], Train [32], Wheat [19], Dubai [32], and Hongkong [32]) are used to test the effectiveness of the MIEA in Fig. 4. Apparently, the MIEA can remarkably unveil the obscured details and recover vivid color information. Deep insight into the mechanisms of the MIEA is

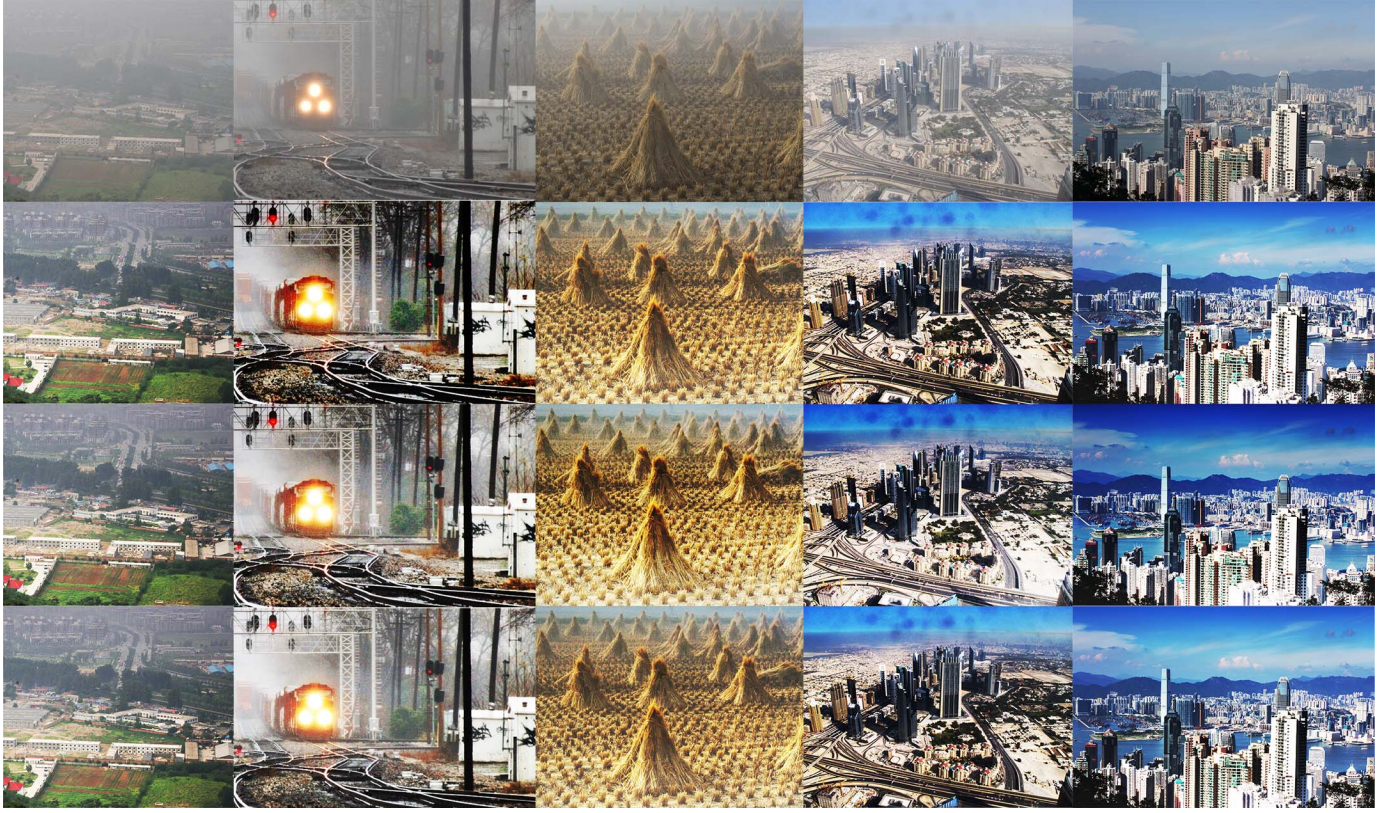


Fig. 4. First column lists the original image (Highway [19], Train [32], Wheat [19], Dubai [32], and Hongkong [32]). The two–fourth columns list the images that are processed by the MIEA (25°C , 35°C , and 75°C).

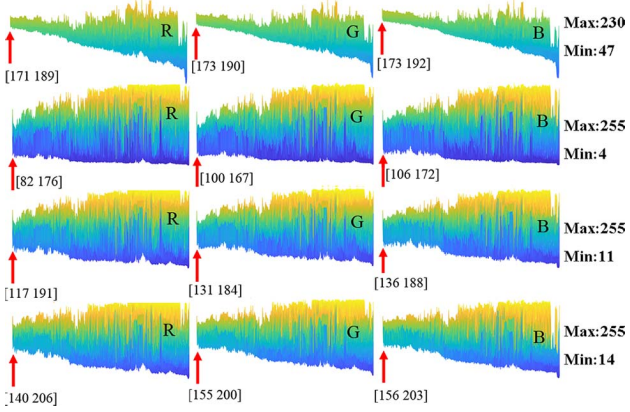


Fig. 5. First column demonstrates the pseudocolor RGB channel of the original image (Highway [19]) in the $Y\text{-}Z$ view. The two–fourth columns exhibit the pseudocolor RGB channel of the image processed by the MIEA in the $Y\text{-}Z$ view at different temperatures (25°C , 35°C , and 75°C).

analyzed, as shown in Fig. 5. In the original image, Highway, the maximum and minimum pixels are 47 and 230, and the pixels, where the red arrow is pointing, distribute in the range [171, 189], [173, 190], and [173, 192] in the R, G, and B channels, respectively. Compare with the original image, in the images, Highway, processed by the MIEA at the temperatures 25°C , 35°C , and 75°C , all the maximum pixel values are pulled up to 255, and the minimum pixel values are pulled down to 4, 11, and 14, respectively. More notably, the pixels

in a small region, such as the regions in the first column where the red arrows are pointing, have been compressed or expanded to some extent, greatly enhancing the contrast. Summarily, Fig. 5 give vivid and concrete descriptions that the MIEA effectively corrects uneven distribution and locally expands the distribution range of the pixels.

Moreover, six no-reference image quality assessment models, including blind/referenceless image spatial quality evaluator (BRISQUE) [33], natural image quality evaluator (NIQE) [34], spatial–spectral entropy-based quality (SSEQ) [35], Minkowski distance-based metric (MDM) [36], contrast enhancement image quality assessment (CEIQ) [37], and blind image quality assessment (NBIQ) [38], are tabulated to evaluate the performance of the MIEA. Table I illustrates the performance of the images (see Fig. 6) using the above six image quality assessments, where the top two are highlighted in bold red font and the first row in bold black font shows the performance of the original image. On the whole, the NBIQ, CEIQ, SSEQ, and BRISQUE of the images processed by the MIEA achieve the best performance, while their MDM and NIQE have slightly worse performance. In the blue rectangles, Fig. 6(b7) shows the best performance, and Fig. 6(b2) and (b4) shows the second best performance. While, in the red rectangles, Fig. 6(c7) still shows the best performance, Fig. 6(c4), (c5), and (c8) shows the second best performance, and Fig. 6(c3) observes the worst performance. This phenomenon is induced by the memristive characteristics in Fig. 2 and the MIEA, where the high-valued pixels in Fig. 6(c1) are

TABLE I
IMAGE QUALITY ASSESSMENT INDEX OF THE IMAGE “HIGHWAY”

Index Type	BRISQUE (a / b / c)			NIQE (a / b / c)			SSEQ (a / b / c)			MDM (a / b / c)			CEIQ (a / b / c)			NBIQ (a / b / c)		
Fig.6(a1)	19.27	24.34	33.63	3.61	9.62	5.01	26.91	17.71	24.71	0.77	0.50	0.72	2.76	1.89	2.21	45.16	32.75	36.96
Fig.6(a2)	17.54	18.19	31.56	2.67	4.98	5.42	8.00	-5.16	14.61	0.95	0.77	0.93	3.60	2.99	3.11	75.48	58.03	65.10
Fig.6(a3)	17.33	14.69	31.65	2.59	5.13	5.14	10.30	-4.39	15.27	0.95	0.80	0.92	3.45	2.75	2.84	72.36	55.80	61.76
Fig.6(a4)	16.70	12.73	30.39	2.69	4.98	5.86	11.56	-4.60	14.45	0.95	0.82	0.93	3.38	2.64	3.12	76.42	52.97	67.40
Fig.6(a5)	19.12	18.18	30.48	2.38	4.26	4.86	26.61	3.14	20.15	0.97	0.71	0.97	3.29	2.85	3.37	69.16	50.11	71.72
Fig.6(a6)	20.09	21.55	30.40	2.43	4.91	4.56	29.41	9.44	20.87	0.97	0.61	0.97	3.22	2.59	3.36	67.89	49.25	72.67
Fig.6(a7)	17.53	12.84	30.37	2.40	4.29	4.69	24.01	-1.77	20.60	0.97	0.97	0.97	3.37	3.18	3.38	70.54	58.75	73.95
Fig.6(a8)	20.42	21.19	31.60	2.44	4.68	4.44	28.75	8.93	20.87	0.97	0.80	0.97	3.23	2.64	3.35	67.87	52.44	72.84



Fig. 6. (a1) Original image and (a2)–(a4) images processed by the MIEA using memristors at different temperatures of 25 °C, 35 °C, and 75 °C, respectively. (a5)–(a8) Images processed by the algorithms [14], [15], [17], and [19], respectively. The local minutiae graphs [the blue rectangle (b1)–(b8) and the red rectangle (c1)–(c8)] are parts of the images (a1)–(a8).

squeezed into a smaller and higher valued range, resulting in an insufficient contrast in Fig. 6(c2)–(c4), and the low-valued pixels in Fig. 6(b1) are held down to the appropriate pixel values by the transmission map, and either the low-valued pixels are brought down to lower values or the high-valued pixels are brought up to higher values, as shown in Fig. 6(b2)–(b4). Meanwhile, the memristive characteristics broaden the range of intermediate valued pixels, tremendously enhancing contrast and significantly improving overall performance. To sum up, the MIEA improves image quality as a whole and achieves comparable performance with classical algorithms.

In addition, the time and energy consumption [2], [11], [39], [40] are analyzed. Compared with classical computationally complex and refined transmission map [17], the MIEA’s first advantage in speed efficiency is the calculation of a coarse transmission map, as shown in Fig. 3, which takes 0.047 s on Intel i7-9700K CPU (14 nm), and the execution time is ninety percent less time than 0.542 s in the [17]. The MIEA’s second advantage in speed efficiency is a simple two-step process, which is of much fewer steps than those in the classical dehazing algorithms. The execution time of the classical algorithm [17] is 0.757 s on Intel i7-9700K CPU (14 nm), and the execution time of the MIEA depends on the set process of a memristor, which is highly related to the migration rate of the hole or oxygen ion. The article [11] reported that any weight-update operation could be completed in 240 ns (90 nm). The division is $0.757 \text{ s} / (2 \times 240 \text{ ns}) = 1.58 \text{ e}^6$, and it is reasonable to assume that the MIEA would have much less execution time than the classical

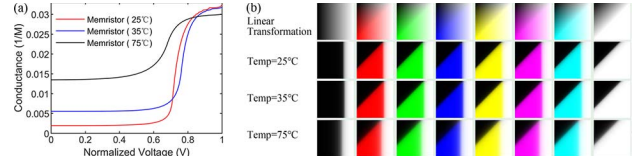


Fig. 7. (a) Conductance changes with the normalized voltage at different temperatures. (b) Variations of the colors (black, red, green, blue, yellow, magenta, cyan, and white) processed by the linear transformation (the first row) and the MIEA (the second-to-fourth rows).

dehazing algorithms. Besides, the main energy consumption in the MIEA is to compute the transmission map (6816 Kb, 0.047 s), which is much less than the energy consumption (21624 Kb, 0.542 s) of the transmission map in the [17]. In the articles [2], [11], the computational energy efficiency exceed those of today’s graphical processing units by two orders of magnitude. Therefore, it is reasonable to assume that the MIEA of less computing operations would have much less energy consumption than the classical dehazing algorithms.

IV. ROBUSTNESS VERIFICATION

Due to uncontrollable formation and annihilation of the CFs, variations, including threshold switching voltage [41] and maximum currents [42], are well-known intractable memristive problems that not only affect memristive characteristics but also deteriorate the performance of memristor-based applications. Although a significant amount of efforts [43], [44] have been put forward to weaken or eliminate the effect of undesirable factors, variations are still inevitable.

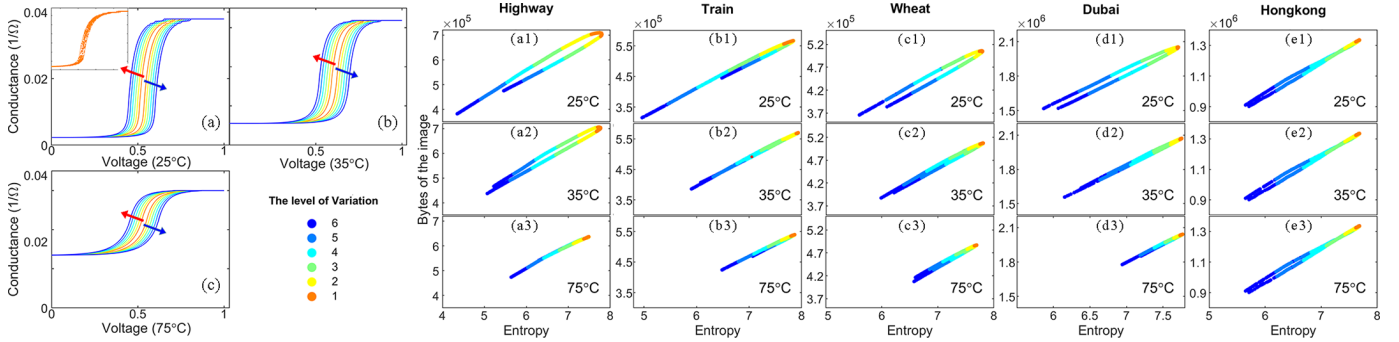


Fig. 8. Conductance of memristors (with the cycle-to-cycle variations) change with the voltages at the temperatures (a) 25 °C, (b) 35 °C, and (c) 75 °C. The bytes of an image [Highway (a1)–(a3), Train (b1)–(b3), Wheat (c1)–(c3), Dubai (d1)–(d3), and Hongkong (e1)–(e3)] in the PNG format and its entropy are illustrated at different temperatures 25 °C, 35 °C, and 75 °C. The inset in (a) is within a small variations (DarkOrange1).

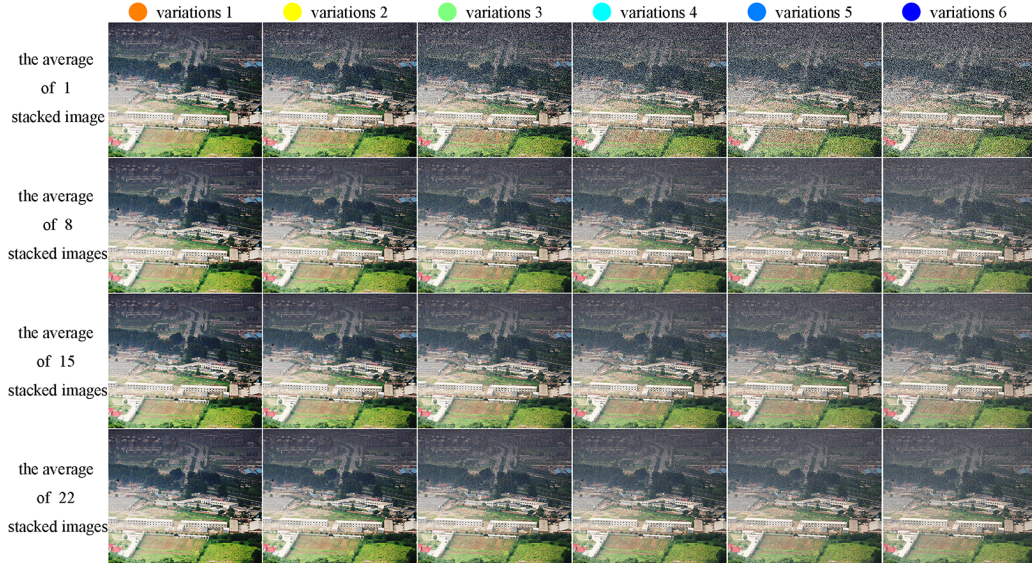


Fig. 9. First–fourth rows show the average of 1, 8, 15, and 22 stacked images processed by the MIEA, respectively. The images in the first–sixth columns are processed by the MIEA using memristors with different variations.

Among these variations, high endurance [4], [10], [40], [41], [45] is necessary for the high-performance MIEA, while the improvement of the device is beyond the scope of this work. To explore the influence of memristors on the MIEA, the temperature effect, the device-to-device, and cycle-to-cycle variations are discussed, and several images are stacked to eliminate memristive variations' effect.

A. Temperature Effect

Temperature affects the MIEA through accelerating molecular motion and further altering memristive characteristics [27], as shown in Fig. 7(a), where the initial maximum memristance (minimum conductance) decreases (increases). To explore how temperature affects the MIEA, param_a (normalized horizontal X-axis) and param_b (normalized vertical Y-axis) are used as the independent variables (parameter space) to shape the mapping relationship of memristor-based voltage-current function (see Fig. 2), whereinto the pixels are first modulated as the voltage V_{v1} and V_{v2} and the output currents are indicated as the corresponding colors (color space) in Fig. 7(b) at different

temperatures (25 °C, 35 °C, and 75 °C). Here, the linear transformation is a control group.

Due to the fact that pixels processed by the MIEA tend to nearest extreme value, the MIEA is apparently superior to the linear transformation on keeping the colors unchanged, and about 47% parameter space keeps the invariability of color space in Fig. 7(b). Specifically, compared with memristors at the temperatures 25 °C and 75 °C, the memristors at the temperature 35 °C have the sharpest change of memristance, resulting in the largest parameter space to keep the invariability of color space. Due to a proper compression of low-valued pixels and high-valued pixels, the method MIEA at the temperature 75 °C achieves much better performance using memristors with a lower slope, as shown in Fig. 6 and Table I.

B. Memristors' Variations

The device-to-device and cycle-to-cycle variations are simulated by updating CFs' lengths, whose variations follow normal distribution [10], [20]. The variations are introduced to the memristors at different temperatures, which are used

in the MIEA to simulate the influence of the cycle-to-cycle (one memristor) variations and device-to-device (different memristors) variations, as shown in Fig. 8(a)–(c). Thereinto, every color either corresponds to memristive characteristic curves between those of the same color in Fig. 8(a)–(c) or corresponds to the quality assessments of 1000 test samples [see Fig. 8(a1)–(e3)]. In Fig. 8, the entropy is a statistical measure of randomness that can be used to characterize the texture of the input image, and the image bytes in portable network graphic (PNG) format take advantage of the facts that the PNG format is entirely lossless and the pixel values in an image can be represented as a difference from the previous value. In the foggy region of a haze image, the difference between adjacent pixels is small, resulting in an image with fewer bytes, establishing a relationship between the image bytes in PNG format and the image quality. As shown in Fig. 8(a1)–(e3) and the first row in Fig. 9, memristors, with the larger variations, exert a more disastrous effect on the MIEA, and only a fraction of memristors within a small variations [DarkOrange1, shown in the inset in Fig. 8(a)], has a negligible and acceptable effect on the MIEA.

Although a large number of efforts [46] have been made at the device level and the system level, various variations usually prevent memristor-based applications from achieving high accuracy. The problem can be addressed to some extent by calculating the average of several stacked images that have been processed by the MIEA, as shown in Fig. 9. With the increase in variations in the memristor, the average of more stacked images cannot solve the problem fundamentally, which can be seen in the fourth row of the images. Besides, the retention degradation and insufficient multistable memristance aggravate the variations and further deteriorate the MIEA. It is noteworthy that this work still provides guidance for memristor-based image processing.

V. CONCLUSION

In this article, a memristor model is modulated to be more accordant with the experimental data at different temperatures. Based on the memristor model, a novel MIEA is proposed, and sufficient quantitative assessments are presented for verifying its performance and robustness. Experimental results show that MIEA strikes a balance between low brightness region and high brightness region and is of simple calculation using a coarse transmission map and an outstanding performance comparable to the classical algorithms. Besides, the influences of temperature effect and device-to-device and cycle-to-cycle variations on MIEA have been discussed, and the average of several stacked images can effectively relieve the influence of variations on the MIEA. We hope that our algorithm can pave a new way for memristor-based image processing and build a bridge between the memristor and memristor-based applications.

ACKNOWLEDGMENT

The numerical calculations in this article are done on the supercomputing system at the Supercomputing Center, Wuhan University.

REFERENCES

- [1] S. Yu, "Neuro-inspired computing with emerging nonvolatile memories," *Proc. IEEE*, vol. 106, no. 2, pp. 260–285, Feb. 2018, doi: [10.1109/JPROC.2018.2790840](https://doi.org/10.1109/JPROC.2018.2790840).
- [2] P. Yao *et al.*, "Fully hardware-implemented memristor convolutional neural network," *Nature*, vol. 577, no. 7792, pp. 641–646, Jan. 2020, doi: [10.1038/s41586-020-1942-4](https://doi.org/10.1038/s41586-020-1942-4).
- [3] Z. Tang *et al.*, "A hardware friendly unsupervised memristive neural network with weight sharing mechanism," *Neurocomputing*, vol. 332, pp. 193–202, Mar. 2019, doi: [10.1016/j.neucom.2018.12.049](https://doi.org/10.1016/j.neucom.2018.12.049).
- [4] S. Salahuddin, K. Ni, and S. Datta, "The era of hyper-scaling in electronics," *Nature Electron.*, vol. 1, no. 8, pp. 442–450, Aug. 2018, doi: [10.1038/s41928-018-0117-x](https://doi.org/10.1038/s41928-018-0117-x).
- [5] S. Kim *et al.*, "NVM neuromorphic core with 64k-cell (256-by-256) phase change memory synaptic array with on-chip neuron circuits for continuous *in-situ* learning," in *IEDM Tech. Dig.*, Washington, DC, USA, Dec. 2015, Art. no. 15800928.
- [6] S. Yu *et al.*, "Binary neural network with 16 mb RRAM macro chip for classification and online training," in *IEDM Tech. Dig.*, San Francisco, CA, USA, Dec. 2016, Art. no. 16651048.
- [7] M. Hu *et al.*, "Memristor-based analog computation and neural network classification with a dot product engine," *Adv. Mater.*, vol. 30, no. 9, Mar. 2018, Art. no. 1705914, doi: [10.1002/adma.201705914](https://doi.org/10.1002/adma.201705914).
- [8] C. Li *et al.*, "Efficient and self-adaptive *in-situ* learning in multilayer memristor neural networks," *Nature Commun.*, vol. 9, no. 1, p. 2385, Jun. 2018, doi: [10.1038/s41467-018-04484-2](https://doi.org/10.1038/s41467-018-04484-2).
- [9] C. Li *et al.*, "Long short-term memory networks in memristor crossbar arrays," *Nature Mach. Intell.*, vol. 1, no. 1, pp. 49–57, Jan. 2019, doi: [10.1038/s42256-018-0001-4](https://doi.org/10.1038/s42256-018-0001-4).
- [10] C. Li *et al.*, "Analogue signal and image processing with large memristor crossbars," *Nature Electron.*, vol. 1, no. 1, pp. 52–59, Dec. 2017, doi: [10.1038/s41928-017-0002-z](https://doi.org/10.1038/s41928-017-0002-z).
- [11] S. Ambrogio *et al.*, "Equivalent-accuracy accelerated neural-network training using analogue memory," *Nature*, vol. 558, no. 7708, pp. 60–67, Jun. 2018, doi: [10.1038/s41586-018-0180-5](https://doi.org/10.1038/s41586-018-0180-5).
- [12] B. Wang, L. L. Chen, and Y. Z. Liu, "New results on contrast enhancement for infrared images," *Optik*, vol. 178, pp. 1264–1269, Feb. 2019, doi: [10.1016/j.jleo.2018.09.165](https://doi.org/10.1016/j.jleo.2018.09.165).
- [13] K. Tan and J. P. Oakley, "Enhancement of color images in poor visibility conditions," in *Proc. Int. Conf. Image Process.*, Vancouver, BC, Canada, 2000, pp. 788–791.
- [14] R. T. Tan, "Visibility in bad weather from a single image," in *Proc. IEEE Conf. Comput. Vis. Pattern Recognit.*, Anchorage, AK, USA, Jun. 2008, Art. no. 10139948.
- [15] J.-P. Tarel, N. Hautiere, L. Caraffa, A. Cord, H. Halmaoui, and D. Gruyer, "Vision enhancement in homogeneous and heterogeneous fog," *IEEE Intell. Transp. Syst. Mag.*, vol. 4, no. 2, pp. 6–20, Apr. 2012, doi: [10.1109/MITS.2012.2189969](https://doi.org/10.1109/MITS.2012.2189969).
- [16] K. Nishino, L. Kratz, and S. Lombardi, "Bayesian defogging," *Int. J. Comput. Vis.*, vol. 98, no. 3, pp. 263–278, Jul. 2012, doi: [10.1007/s11263-011-0508-1](https://doi.org/10.1007/s11263-011-0508-1).
- [17] K. He, J. Sun, and X. Tang, "Single image haze removal using dark channel prior," *IEEE Trans. Pattern Anal. Mach. Intell.*, vol. 33, no. 12, pp. 2341–2353, Dec. 2011, doi: [10.1109/TPAMI.2010.168](https://doi.org/10.1109/TPAMI.2010.168).
- [18] G. Meng, Y. Wang, J. Duan, S. Xiang, and C. Pan, "Efficient image dehazing with boundary constraint and contextual regularization," in *Proc. IEEE Int. Conf. Comput. Vis.*, Sydney, NSW, Australia, Dec. 2013, Art. no. 14144884.
- [19] M. Sulami, I. Glatzer, R. Fattal, and M. Werman, "Automatic recovery of the atmospheric light in hazy images," in *Proc. IEEE Int. Conf. Comput. Photography (ICCP)*, Santa Clara, CA, USA, May 2014, Art. no. 14383045.
- [20] R. Zhu, S. Chang, H. Wang, Q. Huang, J. He, and F. Yi, "A versatile and accurate compact model of memristor with equivalent resistor topology," *IEEE Electron Device Lett.*, vol. 38, no. 10, pp. 1367–1370, Oct. 2017, doi: [10.1109/LED.2017.2736006](https://doi.org/10.1109/LED.2017.2736006).
- [21] R. Zhu *et al.*, "Influence of compact Memristors' stability on machine learning," *IEEE Access*, vol. 7, pp. 47472–47478, 2019, doi: [10.1109/ACCESS.2019.2909295](https://doi.org/10.1109/ACCESS.2019.2909295).
- [22] C. Du, F. Cai, M. A. Zidan, W. Ma, S. H. Lee, and W. D. Lu, "Reservoir computing using dynamic memristors for temporal information processing," *Nature Commun.*, vol. 8, no. 1, p. 2204, Dec. 2017, doi: [10.1038/s41467-017-02337-y](https://doi.org/10.1038/s41467-017-02337-y).

- [23] I. Gupta, A. Serb, A. Khiat, R. Zeitler, S. Vassanelli, and T. Prodromakis, "Real-time encoding and compression of neuronal spikes by metal-oxide memristors," *Nature Commun.*, vol. 7, no. 1, p. 12805, Nov. 2016, doi: [10.1038/ncomms12805](https://doi.org/10.1038/ncomms12805).
- [24] Y. Yang, P. Gao, S. Gaba, T. Chang, X. Pan, and W. Lu, "Observation of conducting filament growth in nanoscale resistive memories," *Nature Commun.*, vol. 3, no. 1, p. 732, Mar. 2012, doi: [10.1038/ncomms1737](https://doi.org/10.1038/ncomms1737).
- [25] J. J. Yang, D. B. Strukov, and D. R. Stewart, "Memristive devices for computing," *Nature Nanotechnol.*, vol. 8, no. 1, pp. 13–24, Jan. 2013, doi: [10.1038/nnano.2012.240](https://doi.org/10.1038/nnano.2012.240).
- [26] R. Waser and M. Aono, "Nanoionics-based resistive switching memories," *Nature Mater.*, vol. 6, no. 11, pp. 833–840, Nov. 2007, doi: [10.1038/nmat2023](https://doi.org/10.1038/nmat2023).
- [27] L. Goux, J. Lisoni, M. Jurczak, D. Wouters, L. Courtade, and C. Müller, "Coexistence of the bipolar and unipolar resistive-switching modes in NiO cells made by thermal oxidation of Ni layers," *J. Appl. Phys.*, vol. 107, no. 2, p. 785, Nov. 2010, doi: [10.1063/1.3275426](https://doi.org/10.1063/1.3275426).
- [28] Y. N. Joglekar and S. J. Wolf, "The elusive memristor: Properties of basic electrical circuits," *Eur. J. Phys.*, vol. 30, no. 4, pp. 661–675, May 2009, doi: [10.1088/0143-0807/30/4/001](https://doi.org/10.1088/0143-0807/30/4/001).
- [29] T. Prodromakis, B. P. Peh, C. Papavassiliou, and C. Toumazou, "A versatile memristor model with nonlinear dopant kinetics," *IEEE Trans. Electron Devices*, vol. 58, no. 9, pp. 3099–3105, Sep. 2011, doi: [10.1109/TED.2011.2158004](https://doi.org/10.1109/TED.2011.2158004).
- [30] D. B. Strukov, G. S. Snider, D. R. Stewart, and R. S. Williams, "The missing memristor found," *Nature*, vol. 453, no. 7191, pp. 80–83, May 2008, doi: [10.1038/nature06932](https://doi.org/10.1038/nature06932).
- [31] R. Fattal, "Single image dehazing," *ACM Trans. Graph.*, vol. 27, no. 3, pp. 1–9, Aug. 2008, doi: [10.1145/1360612.1360671](https://doi.org/10.1145/1360612.1360671).
- [32] R. Fattal, "Dehazing using color-lines," *ACM Trans. Graph.*, vol. 34, no. 1, pp. 1–14, Dec. 2014, doi: [10.1145/2651362](https://doi.org/10.1145/2651362).
- [33] A. Mittal, A. K. Moorthy, and A. C. Bovik, "No-reference image quality assessment in the spatial domain," *IEEE Trans. Image Process.*, vol. 21, no. 12, pp. 4695–4708, Dec. 2012, doi: [10.1109/TIP.2012.2214050](https://doi.org/10.1109/TIP.2012.2214050).
- [34] A. Mittal, R. Soundararajan, and A. C. Bovik, "Making a 'Completely Blind' image quality analyzer," *IEEE Signal Process. Lett.*, vol. 20, no. 3, pp. 209–212, Mar. 2013, doi: [10.1109/LSP.2012.2227726](https://doi.org/10.1109/LSP.2012.2227726).
- [35] L. Liu, B. Liu, H. Huang, and A. C. Bovik, "No-reference image quality assessment based on spatial and spectral entropies," *Signal Process., Image Commun.*, vol. 29, no. 8, pp. 856–863, Sep. 2014, doi: [10.1016/j.image.2014.06.006](https://doi.org/10.1016/j.image.2014.06.006).
- [36] H. Ziae Nafchi and M. Cheriet, "Efficient no-reference quality assessment and classification model for contrast distorted images," *IEEE Trans. Broadcast.*, vol. 64, no. 2, pp. 518–523, Jun. 2018, doi: [10.1109/TBC.2018.2818402](https://doi.org/10.1109/TBC.2018.2818402).
- [37] J. Yan, J. Li, and X. Fu, "No-reference quality assessment of contrast-distorted images using contrast enhancement," 2019, *arXiv:1904.08879*. [Online]. Available: <http://arxiv.org/abs/1904.08879>
- [38] F.-Z. Ou, Y.-G. Wang, and G. Zhu, "A novel blind image quality assessment method based on refined natural scene statistics," in *Proc. IEEE Int. Conf. Image Process. (ICIP)*, Taipei, Taiwan, Sep. 2019, pp. 1004–1008, doi: [10.1109/ICIP.2019.8803047](https://doi.org/10.1109/ICIP.2019.8803047).
- [39] W. Zhang *et al.*, "Neuro-inspired computing chips," *Nature*, vol. 3, no. 7, pp. 371–380, Jul. 2020, doi: [10.1038/s41928-020-0435-7](https://doi.org/10.1038/s41928-020-0435-7).
- [40] Q. Xia and J. J. Yang, "Memristive crossbar arrays for brain-inspired computing," *Nature Mater.*, vol. 18, no. 4, pp. 309–323, Mar. 2019, doi: [10.1038/s41563-019-0291-x](https://doi.org/10.1038/s41563-019-0291-x).
- [41] Z. Wang *et al.*, "Memristors with diffusive dynamics as synaptic emulators for neuromorphic computing," *Nature Mater.*, vol. 16, no. 1, pp. 101–108, Jan. 2017, doi: [10.1038/nmat4756](https://doi.org/10.1038/nmat4756).
- [42] V. K. Sangwan *et al.*, "Multi-terminal memtransistors from polycrystalline monolayer molybdenum disulfide," *Nature*, vol. 554, no. 7693, pp. 500–504, Feb. 2018, doi: [10.1038/nature25747](https://doi.org/10.1038/nature25747).
- [43] R. Cao *et al.*, "Improvement of device reliability by introducing a BEOL-compatible TiN barrier layer in CBRAM," *IEEE Electron Device Lett.*, vol. 38, no. 10, pp. 1371–1374, Oct. 2017, doi: [10.1109/LED.2017.2746738](https://doi.org/10.1109/LED.2017.2746738).
- [44] S. Srivastava, P. Dey, S. Asapu, and T. Maiti, "Role of GO and r-GO in resistance switching behavior of bilayer TiO₂ based RRAM," *Nanotechnology*, vol. 29, no. 50, Oct. 2018, Art. no. 505702, doi: [10.1088/1361-6528/aae135](https://doi.org/10.1088/1361-6528/aae135).
- [45] E. Cha *et al.*, "Nanoscale (~10 nm) 3D vertical ReRAM and NbO₂ threshold selector with TiN electrode," in *IEDM Tech. Dig.*, Washington, DC, USA, 2013, pp. 10–15, doi: [10.1109/IEDM.2013.6724602](https://doi.org/10.1109/IEDM.2013.6724602).
- [46] D. Joksa *et al.*, "Committee machines—A universal method to deal with non-idealities in memristor-based neural networks," *Nature Commun.*, vol. 11, no. 1, p. 4273, Dec. 2020, doi: [10.1038/s41467-020-18098-0](https://doi.org/10.1038/s41467-020-18098-0).